International Journal of Heat and Mass Transfer 184 (2022) 122171

Contents lists available at ScienceDirect

International Journal of Heat and Mass Transfer

journal homepage: www.elsevier.com/locate/hmt

Study on the transition behavior of the bulging effect during deep penetration laser beam welding

Antoni Artinov[a,*], Xiangmeng Meng[b], Marcel Bachmann[a], Michael Rethmeier[b,a,c]

[a] Bundesanstalt für Materialforschung und prüfung (BAM), Unter den Eichen 87, 12205 Berlin, Germany
[b] Institute of Machine Tools and Factory Management, Technische Universität Berlin, Pascalstrae 8-9, 10587 Berlin, Germany
[c] Fraunhofer Institute for Production Systems and Design Technology, Pascalstrae 8-9, 10587 Berlin, Germany

ARTICLE INFO

Article history:
Received 5 July 2021
Revised 5 October 2021
Accepted 22 October 2021
Available online 9 December 2021

Keywords:
Laser beam welding
Deep penetration
Bulge formation
Numerical modeling

ABSTRACT

The present work is devoted to the study of the transition behavior of the recently confirmed widening of the weld pool, known as the bulging effect, during high-power deep penetration laser beam welding of thick unalloyed steel sheets. A three-dimensional transient multi-physics numerical model is developed, allowing for the prediction of the bulge formation and the study of its temporal behavior. The model is generalized to account automatically for the transition from partial to complete penetration. Several experimental measurements and observations, such as drilling period, weld pool length, temperature, efficiency, and metallographic cross-sections are used to verify the model and assure the plausibility of the numerical results. The analysis of the calculated temperature and velocity distributions, as well as the evolution of the keyhole geometry, shows that the formation of a bulging region strongly depends on the penetration depth of the weld. Based on the numerical results, the bulge is found to occur transiently, having its transition from a slight bulge to a fully developed bulging between penetration depths of 6 mm and 9 mm, respectively.

1. Introduction

In the last decade the development of modern laser systems with high-power of up to 100 kW for solid state lasers enabled joining sheets with a thickness of up to 50 mm by a single pass welding [1–3]. Nowadays, the laser beam welding process brings several technical advantages compared to conventional arc welding processes, such as low distortion of the welded components due to the locally highly concentrated and precise heat input, high reachable welding speed, narrow heat affected zone, etc. [4]. Hence, the application of the laser beam welding process on sheets of higher thickness offers a great potential for more effective joining, e.g., by the production of high pressure and vacuum vessels, crane construction, as well as in the shipbuilding and aerospace industry.

However, with the increase of welding speed and sheet thickness, new challenges arise, such as untypical defect formation for specific materials, e.g., hot-cracking during welding of unalloyed and low-alloyed steel sheets [5–7]. Although, hot-cracking is one of the most studied material phenomena from the welding field, its nature remains highly complex [8,9]. Nevertheless, it is a well-known fact that the interaction between the three crucial factors, namely the thermal, mechanical, and metallurgical factor, is decisive for the cracking susceptibility of the welded specimen [10]. Hereby, their interaction is strongly dependent on the weld pool shape and vice versa, see, e.g., [11]. The importance of this dependency was demonstrated back in the early 1980s during studies on deep penetration electron beam welding. In these studies, a geometric particularity, or more precisely a local disturbance of the solidification front was observed in the longitudinal section of the welded specimen by adding a pure Ni-wire at different positions along the thickness of the specimen. The disturbance led to a local delay in the solidification behavior, which led to an increase in the cracking sensitivity of the welded component [12–15]. To the best of the author's knowledge, there are only a few research results published on the occurrence of the widening of the weld pool interface during welding with high power lasers, nowadays referred to as the bulging effect. In more recent studies, sophisticated modern visualization techniques combining transparent

* Corresponding author.
E-mail address: Antoni.Artinov@bam.de (A. Artinov).

https://doi.org/10.1016/j.ijheatmasstransfer.2021.122171

Table 1
Standardized and measured chemical composition of the materials used in wt%.

Material	C	Si	Mn	P	S	Cu	Fe
EH36-N	0.132	0.26	1.4	-	-	0.012	bal.
S355J2+N	0.088	0.34	1.38	-	-	0.028	bal.
DIN EN 10025	≤0.2	≤0.55	≤1.6	≤0.025	≤0.035	≤0.55	bal.

quartz glass with high speed imaging and thermal camera recording have been utilized to overcome the limited experimental accessibility and capture the transient behavior of the bulging effect [11,16]. Furthermore, attempts to quantify the bulge during hybrid laser-gas metal arc welding by defining an angle determined from the narrowest and widest cross-sectional dimensions within the bulging region has been made in [17,18]. Although the latest research proves the existence of the bulging effect during laser beam welding of thick sheets, the obtained data does not allow for a complete investigation or quantification of the weld pool widening, e.g., the study of its formation mechanisms or its influence on crucial factors for the formation of defects.

In the present time, due to the rising computational performance, numerical simulations have brought significant insights into the investigation of complex phenomena. Even though not being the object of investigation, the bulging effect can be found in several numerical works, see, e.g., [19–25]. Its influence on the mechanical factor, or more precisely on the temporal strain/stress evolution in the critical bulging region, has been studied in [7,26]. Further development on this study has been achieved by making use of the equivalent heat source (EHS) technique proposed first in [27], see, e.g., [28,29]. The EHS approach enables the precise coupling of the weld pool shape predicted with a thermo-fluid dynamics simulation and the subsequent thermo-mechanical computation [30,31]. An overview of the relationship between the bulging effect and the hot cracking formation during deep penetration laser beam welding, where all three critical factors are considered, can be found in the author's previous study, see [32]. In their study, the authors emphasize on the interaction between the bulge and the extended solidification temperature range due to the accumulation of elements constituting low melting eutectic, such as sulfur and phosphorous, and their segregation. As described above and in [33,34], such solidification delay has already been found to decrease the cracking resistivity of the welded component.

Based on the literature review it can be concluded that the bulging effect plays a crucial role in the formation of defects during deep penetration laser beam welding. Yet, the majority of numerical works published on this topic either do not study the bulging phenomenon at all or rather concentrate on its phenomenological reproduction to estimate its influence on critical factors, such as the three main factors determining the cracking susceptibility of the specimen mentioned above. Hence, further numerical analysis of this phenomenon is essential for the understanding of the laser process and the setting of the relevant process parameters.

The present study seeks to deepen the level of understanding by emphasizing on the formation of the bulge and more specifically on its correlation to the penetration depth of the weld. Thus, an effort is made to develop a three-dimensional transient multi-physics numerical model taking into account the most important physical phenomena, such as dynamic keyhole evolution, energy absorption by laser reflections, vaporization, thermo-capillary, and natural convection, latent heat of phase transformations, and temperature-dependent material properties. Furthermore, an extensive amount of experimental data is measured to fully verify the predictions made by the model.

Table 2
Process parameters of the experiments.

Parameters	Value		
Wave length	1030 nm		
Fibre diameter	200 μm		
Beam parameter product (BPP)	8 mm mrad		
Optical system	HIGHYAG BIMO HP		
Focal diameter	500 μm		
Focal length	300 mm		
Rayleigh length	6.9 mm		
Material	EH36-N		S355J2+N
Penetration	partial	complete	partial
Sheet thickness	8 mm	8 mm	12 mm
Laser power	5 kW	8 kW	8 kW
Focal position	0 mm		
Welding speed	2 m min^{-1}		
Laser torch angle	0°		
Shielding gas nozzle angle	35°		
Shielding gas	Ar, 25 l min^{-1}		

2. Materials and Methods

2.1. Materials

Two kinds of unalloyed steel sheets with different thicknesses were utilized in the welding experiments; a 8 mm thick high strength steel for ship structures EH36-N and a 12 mm thick structural steel S355J2+N. The dimensions of the EH36-N and S355J2+N sheets were 300 mm x 100 mm x 8 mm and 175 mm x 100 mm x 12 mm, respectively. The corresponding chemical compositions were measured with spectral analysis and are given in Table 1.

2.2. Experiments

A 16 kW disc laser Trumpf 16002, a diode laser illumination, and a FASTCAM SA4 high speed camera from Photron were utilized in the experiments. Note that the experiments have been especially designed to obtain a sufficient amount of data for the calibration of the model and the validation of the numerically obtained weld pool geometries and fluid flow patter therein, which determine the formation and the dimensions of the bulging region. All welds produced in the experiments were bead-on-plate welds. A schema of the experimental setup is shown in Fig. 1; the process parameters are summarized in Table 2.

The high speed camera was set at 1000 frames per second and the laser power of the diode laser to 200 W. Altogether the experiments have been divided into three parts. First, an estimation of the drilling time for the complete penetration welding process on 8 mm thick EH36-N sheets has been obtained. For this measurement, the lens optical axis of the high speed camera was placed to be perpendicular to the longitudinal section of the sheet. Thus, allowing to capture the very first laser reflection on the top surface and the moment when the laser light goes through the completely penetrated keyhole on the bottom surface. Thermocouples were positioned along the weld centerline as shown in Fig. 2a). Thereby, one thermocouple was placed on the top surface of the specimen to trigger the measurement and three further thermo-

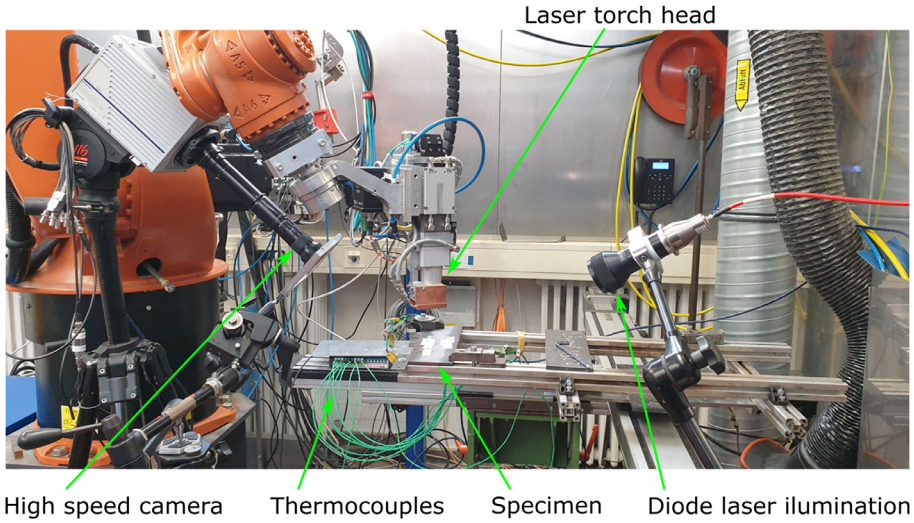

Fig. 1. Schema of the experimental setup.

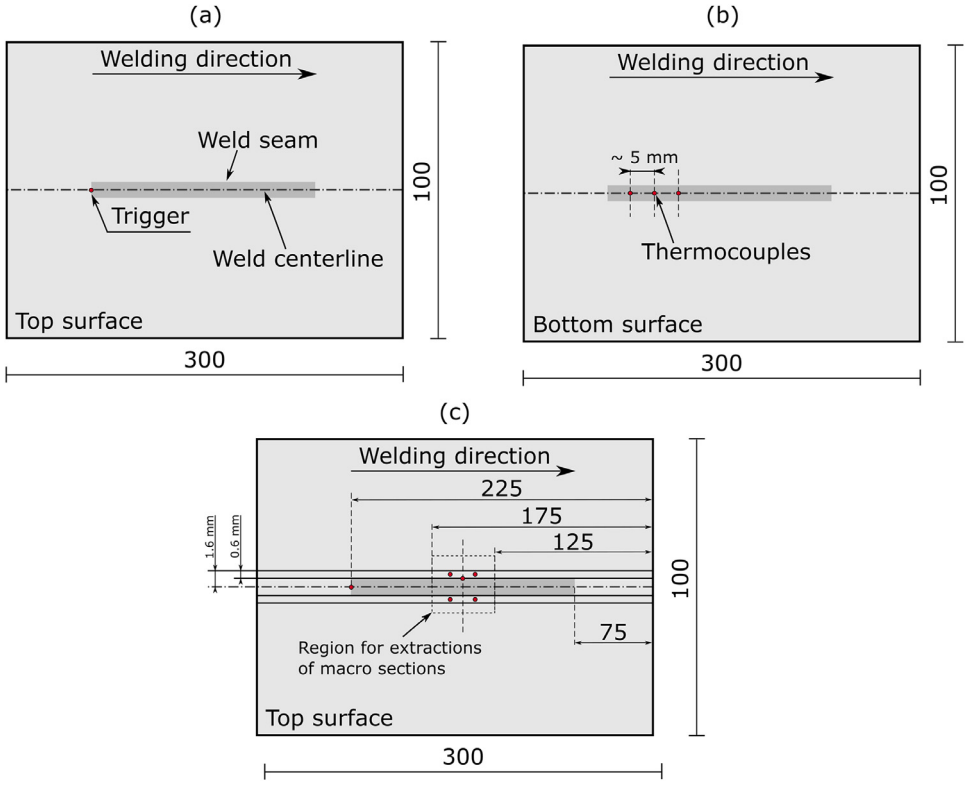

Fig. 2. Position of the thermocouples for the measurement of the: (a)-(b) laser drilling time and (c) time-temperature curves.

couples with a distance of approximately 5 mm were placed on the bottom surface to measure the time temperature curves. According to the measured curves the moment of reaching complete penetration has been estimated. This part of the experiment was repeated three times to get an accurate averaged value of the drilling period.

In the second part of the experiment, the partial penetration welds on the same specimens were performed. During welding, the weld pool length on the top surface was recorded by the high speed camera and the thermal history at several locations was measured by thermocouples, see Fig. 2b). The thermocouples used in the investigation were of type K with a diameter of 0.25 mm. Their exact positions were measured after the welding process with an optical microscope. It is worth noting that preliminary experiments have been performed to estimate the region where the thermocouples should be placed as well as to get an estimation about the thickness above which the bulging effect becomes visible. In the last part of the experiments the 12 mm thick S355J2+N sheets were welded without additional measurements. Macro sections have been extracted from the region marked in Fig. 2c) for the sheets welded in the second and third part of the experiments. From these, several metallographic cross-sections have been prepared with a 2% nital etching, which subsequently have been compared to the numerical results.

2.3. Numerical modelling

A three-dimensional thermo-fluid dynamics model accounting for the free surface tracking by the volume of fluid (VOF) approach has been developed for the prediction of the bulge formation. The model is based on several previous works with some further improvements and adaptions. More details can be obtained from [35–39].

2.3.1. Assumptions

Although, in modern time the computational capacity has been allowing for the numerical analysis of more complex tasks, still severe simplifications need to be made in order to obtain a solution in a feasible computational time. Another reason for the simplifications made in the model is the complex physics behind the laser beam welding process including a number of strongly coupled, highly-nonlinear interactions between the laser radiation, the vapor phase, the molten metal, and the solid material. The main assumptions made in the simulation are summarized as follows:

- The molten metal is assumed to be Newtonian and incompressible, whereby the flow regime of the liquid metal is considered to be laminar.
- The flow regime of the vapor phase in the keyhole is assumed to be laminar.
- The Boussinesq approximation is used to model the impact of the density deviation caused by the temperature difference on the flow.

2.3.2. Governing equations

The governing equations describing the multi-physics model in a fixed Cartesian coordinate system are given below. The VOF technique is employed to track the transient deformation of the molten pool free surface and solidified weld seam profile.

- Volume fraction conservation

$$\frac{\partial \alpha_{vol_{steel}}}{\partial t} + \nabla \cdot \left(\vec{v}\alpha_{vol_{steel}}\right) = 0, \tag{1}$$

where $\alpha_{vol_{steel}}$ denotes the volume fraction of the steel phase in a control volume and $\vec{v} = (v_x, v_y, v_z)$ is the fluid velocity vector. There are three possible conditions for the control volume defined by the volume fraction of the steel, namely a control volume containing only the air phase, $\alpha_{vol_{steel}} = 0$, a control volume containing only the steel phase, $\alpha_{vol_{steel}} = 1$, and a mixture control volume containing the interface between the steel and the air phases, $0 < \alpha_{vol_{steel}} < 1$. Note that the volume fraction conservation equation is solved only for the steel phase; the volume fraction of the air phase is computed based on the following constraint:

$$\sum_{i=1}^{2} \alpha_{vol_i} = 1, \tag{2}$$

where the subscript, $i = 1$, denotes the steel phase and, $i = 2$, the air phase [40]. The steel-air interface is reconstructed using a piecewise-linear approach, assuming that the interface has a linear slope within each control volume [41]. The free surface of the molten pool and the solidified weld is approximated with volume fraction values between 0.2 and 1 and empirically determined critical volume fraction gradient value.

- Mass conservation

$$\nabla \cdot \vec{v} = 0. \tag{3}$$

Note that the density is not appearing in the equation due to the assumptions made above.

- Momentum conservation

A single momentum equation is solved throughout the computational domain. Thus, the resulting velocity field is shared among the phases and the material properties in each cell are averaged by the volume fraction, e.g., the density is calculated as follows:

$$\rho_{mix} = \alpha_{vol_{steel}}\rho_{steel} + \left(1 - \alpha_{vol_{steel}}\right)\rho_{air}, \tag{4}$$

where ρ_{mix} is the volume-fraction-averaged density; ρ_{air} and ρ_{steel} are the densities of the air and steel phases, respectively. All other properties except the thermal expansion coefficient, for example, the viscosity or thermal conductivity, are computed in this manner. Thus, the momentum equation reads:

$$\rho_{mix}\left(\frac{\partial \vec{v}}{\partial t} + (\vec{v}\cdot\nabla)\vec{v}\right) = -\nabla p + \mu_{mix}\nabla^2\vec{v} + \rho_{mix}\vec{g} + \vec{S}_m, \tag{5}$$

where t is the time, p is the fluid pressure, μ_{mix} is the dynamic viscosity, $\vec{g}$ is the gravitational acceleration vector, and $\vec{S}_m$ is the source term. The source term is defined as follows:

$$\vec{S}_m = -\rho_{steel}\vec{g}\beta_{steel}\left(T - T_{liq}\right) + \frac{\left(1-\alpha_{liq}\right)^2}{\left(\alpha_{liq}^3 + \epsilon\right)}A_{mush}\vec{v} + \vec{S}_{surf.tension} + \vec{S}_{rec} + \vec{S}_{vapor}, \tag{6}$$

where β_{steel} is the thermal expansion coefficient, T is the temperature, T_{liq} is the liquidus temperature of the unalloyed steel taken as the reference temperature here, α_{liq} is the liquid volume fraction, ϵ is a small number (1×10^{-3}) used to avoid division by zero, and A_{mush} is the mushy zone constant.

The first term on the right hand side (RHS) describes the thermal buoyancy due to the variations of the density of the steel with temperature [42]. The second term on the RHS describes the deceleration of the flow in the mushy zone which is related to the inverse of the size of the interdendritic structure. Thereby, the mushy zone constant A_{mush} is a measure for the amplitude of the damping, thus it should be very large (in the current study the value is $\sim 5 \times 10^7\,\mathrm{kg\,m^{-3}\,s^{-1}}$) to allow for a steeper transition of the velocity of the material to zero as it solidifies [43,44]. The liquid fraction α_{liq} reads:

$$\alpha_{liq} = \begin{cases} 0 & \text{for} \quad T \le T_{sol} \\ \frac{T - T_{sol}}{T_{liq} - T_{sol}} & \text{for} \quad T_{sol} < T < T_{liq}, \\ 1 & \text{for} \quad T \ge T_{liq} \end{cases} \tag{7}$$

where T_{sol} denotes the solidus temperature of the material used. Additionally, the effective viscosity approach is used to model the flow in the mushy zone. Therefore, the mushy zone is divided into three subregions depending on the coherent solid fraction $F_c = 0.48$ and the critical solid fraction $F_{cr} = 0.64$. Note that the drag coefficient and the local viscosity differ in each region. The local effective viscosity is expressed as a function of the solid fractions [45]:

$$\mu_{steel} = \mu_0\left(1 - \frac{F_s}{F_{cr}}\right)^{-1.55}, \quad \text{for} \quad F_s \neq F_{cr}, \tag{8}$$

where μ_0 is the dynamic viscosity at T_{liq} and F_s is the solid fraction. Note that the local viscosity value in control volumes with a solid fraction higher than the critical solid fraction was set to 200 Pas. The third term in Eq. 6 includes the effects of surface tension along the steel-air interface. Thereby, the tangential stress terms, also known as the Marangoni stress, arising due to the variation of the surface tension are expressed as:

$$\tau_{Ma} = \frac{\partial \gamma}{\partial T}\frac{\partial T}{\partial \vec{t}}, \tag{9}$$

where γ is the surface tension and $\vec{t}$ is the surface unit tangential vector. The surface tension is expressed as [46]:

$$\gamma = \gamma_0 - \hat{A}\left(T - T_{liq}\right) - R_g T \Gamma_s \ln\left(1 + K_s a_s\right), \quad \text{with} \quad K_s = k_l \exp\left(\frac{-\Delta H_0}{R_g T}\right), \tag{10}$$

where γ_0 is the surface tension of the pure metal (in the present study this is iron), $\hat{A}$ is the negative slope of γ as function of the temperature, R_g is the universal gas constant, Γ_s is the surface excess at saturation, a_s is the thermodynamic activity, k_l is a constant related to the entropy of segregation, and ΔH_0 is the standard heat of adsorption. Note that the value for the thermodynamic activity was taken as the maximum allowed value according to the standard given in Table 1. The pressure difference along the steel-air interface, known as the Laplace pressure or the capillary pressure is given as:

$$p_{ca} = \gamma \kappa, \tag{11}$$

with $\kappa = \nabla \cdot \vec{n}$ defined as the curvature in terms of the divergence of the surface unit normal vector, $\vec{n} = \frac{\vec{n}}{|\vec{n}|}$; $\vec{n} = \nabla \alpha_{vol_{steel}}$ is the inward surface normal vector defined as the gradient of the volume fraction of the steel phase. The forces acting on the steel-air interface are expressed as volume forces using the divergence theorem according to the continuum surface force (CSF) model [47]. Therefore, a transformation term is defined as follows:

$$CSF_{momentum} = \frac{\rho_{mix} |\nabla \alpha_{vol_{steel}}|}{\frac{1}{2}(\rho_{air} + \rho_{steel})}, \tag{12}$$

allowing to compute the volume force as:

$$\vec{S}_{surf.tension} = (p_{ca} CSF_{momentum}) \vec{n}. \tag{13}$$

The fourth term in Eq. 6 describes one of the main driving forces on the keyhole surface, namely the evaporation-induced recoil pressure. The recoil pressure is calculated according to [48] and transferred to a volume force as follows:

$$p_{rec} = \frac{A B_0}{\sqrt{T}} \exp\left(-\frac{M_{mol} h_v}{R_g T}\right), \quad \vec{S}_{rec} = (p_{rec} CSF_{momentum}) \vec{n}, \tag{14}$$

where A is numerical coefficient depending on the ambient pressure and its value is approximately $0.55\sqrt{\text{K}}$ for practical applications; B_0 is a vaporization constant, which in the case of iron equals $3.9 \times 10^12\,\text{kg m}^{-1}\,\text{s}^{-2}$; M_{mol} is the molar mass, and h_v is the latent heat of vaporization. The fifth term on the RHS of Eq. 6 includes empirical formulations of the vapor-induced stagnation pressure p_{vapor} and shear stress τ_{vapor}, based on the assumption of a laminar flow within the keyhole [49]. According to [19] these read:

$$p_{vapor} = p_0 + \frac{1}{2} \rho_{vapor} |\vec{v}_{\vec{n}}|^2, \tag{15}$$

$$\tau_{vapor} = \frac{1}{8} f \rho_{vapor} |\vec{v}_{\vec{t}}|^2, \tag{16}$$

where p_0 is the vapor or atmospheric pressure, ρ_{vapor} is the metallic vapor density calculated with the ideal gas equation, $\vec{v}_{\vec{n}}$ and $\vec{v}_{\vec{t}}$ are the normal and tangential projections of the vapor velocity vector, $\vec{V}$, on the steel-air interface, respectively, and $f = 64/\text{Re}$. In the present work, the metallic vapor velocity vector acts vertically in thickness direction and is assumed to have a magnitude of 150 ms^{-1} at the keyhole entrance [50]. Furthermore, the vapor velocity is defined as a function of the penetration/keyhole depth, h_{depth}, increasing linearly from 0 ms^{-1} at the keyhole bottom to its maximum value at the keyhole entrance in the partial penetration case. Note that in the complete penetration case, there are two metallic vapor velocity vectors acting in opposite directions. In this case, one vector increases linearly, starting at two-thirds of the plate thickness, reaching 150 ms^{-1} at the keyhole entrance and a second vector increasing in the same manner towards the keyhole exit, reaching 100 ms^{-1} at the sheet bottom [51,52]. The projection of the vapor velocity vector onto the surface unit normal vector, $\vec{n}$, of the steel-air interface can be calculated as follows:

$$\vec{v}_{\vec{n}} = \left(\vec{V} \cdot \vec{n}\right) \vec{n}. \tag{17}$$

The tangential projection of the vapor velocity can then be calculated by the following vector equation:

$$\vec{v}_{\vec{t}} = \vec{V} - \vec{v}_{\vec{n}}. \tag{18}$$

Equation 16 is further simplified by substituting the Re number and f into it:

$$\tau_{vapor} = \frac{8 \mu_{T_{max}} |\vec{v}_{\vec{t}}|}{D}, \tag{19}$$

where D is the averaged diameter of the keyhole and $\mu_{T_{max}}$ is the dynamic viscosity at the maximum reachable temperature set in the model. For the calculation of D, the keyhole volume, V_{key}, is approximated as a cylindrical pipe with the length of the keyhole depth, h_{depth}, leading to:

$$D = \sqrt{\frac{4 V_{key}}{h_{depth} \pi}}. \tag{20}$$

The dynamic viscosity at T_{max} is approximated by the kinematic theory of gases as follows:

$$\mu_{T_{max}} = \frac{M_{mol}}{3\sqrt{2}\hat{\sigma}} \sqrt{\frac{8 k_b T_{max}}{\pi M_{mol}}}, \tag{21}$$

where $\hat{\sigma} = \pi d_{mol}^2$ is the collision cross-section of the molecule with d_{mol} the molecular diameter and k_b is the Boltzmann constant. In the particular case of the unalloyed steel utilized in this study, see Table 1, the value of the dynamic viscosity is approximately $1.62 \times 10^{-4}\,\text{kg m}^{-1}\,\text{s}^{-1}$ for a super-heating temperature of 3400 K [53,54]. Finally, the corresponding source term can be given as follows:

$$\vec{S}_{vapor} = \vec{S}_{stagnation} + \vec{S}_{shear}, \quad \text{with} \quad \vec{S}_{stagnation} = (p_{vapor} CSF_{momentum}) \vec{n}, \quad \text{and} \quad \vec{S}_{shear} = (\tau_{vapor} CSF_{momentum}) \vec{t}. \tag{22}$$

The CSF method is applied here for the transformation of the stagnation pressure and the shear stress to volume forces according to [55].

- Energy conservation

$$\rho_{mix}\left(\frac{\partial H_{mix}}{\partial t} + (\vec{v} \cdot \nabla) H_{mix}\right) = \nabla \cdot (\lambda_{mix} \nabla T) + S_e, \tag{23}$$

where H_{mix} is the enthalpy, λ_{mix} is the heat conductivity, and S_e is the source term. The enthalpy of the material is computed as the sum of the sensible enthalpy, h_{mix}, and the latent heat of fusion of the material used, h_f, as follows:

$$H_{mix} = h_{mix} + h_f, \tag{24}$$

with h_{mix} given as:

$$h_{mix} = h_{ref} + \int_{T_{ref}}^{T} c_{p_{mix}} dT. \tag{25}$$

Here, the subscript, ref, stands for reference, thus h_{ref} is the reference enthalpy and T_{ref} is the reference temperature; $c_{p_{mix}}$ is the specific heat at constant pressure. Furthermore, the latent heat content, L, in each control volume, is written in terms of the la-

tent heat of the material and the liquid fraction:

$$h_f = \alpha_{liq} L, \tag{26}$$

varying between zero in the solid region and L in the liquid region [43]. The source term is defined as:

$$S_e = S_{laser} + S_{convection} + S_{radiation} + S_{evaporation} + S_{recondensation}. \tag{27}$$

The laser heat flux density is assumed to have a Gaussian-like axis-symetric distribution expressed as [19]:

$$q_L(x,y) = \frac{2P_L}{\pi r_{f0}^2} \exp\left(-2\frac{x^2+y^2}{r_{f0}^2}\right), \tag{28}$$

where P_L is the laser power and r_{f0} is the laser beam radius at the focal plane. The three-dimensional energy distribution is obtained by a self-consistent ray tracing approach proposed in [19], accounting for the multiple reflections and the Fresnel absorption on the keyhole surface. For this, the laser beam is divided into 755 sub-rays, by discretizing the laser spot in the focal plane by 31×31 sub-regions with a length of $D_{sub} = \frac{2r_{f0}}{31}$. Thus, each sub-ray has its own location-dependent energy density. The power of each sub-ray is calculated by the multiplication of the corresponding sub-ray power density and the surface area of the sub-region beneath it:

$$P_{ray}(x,y) = q_L(x,y)\left(\frac{r_{f0}}{31}\right)^2. \tag{29}$$

The initial path of each sub-ray is defined by the diffraction of the laser beam. Therefore, the laser beam radius along the optical axis is approximated as:

$$r_f(z) = r_{f0}\left(1 + \left(\frac{z-z_0}{z_r}\right)^2\right), \tag{30}$$

where z_0 is the position of the focal plane and z_r is the Rayleigh length. The reflection direction vector, $\vec{R}_i$, of the i-th reflection is calculated by the following vector equation:

$$\vec{R}_i = \vec{R}_{i-1} - 2\left(\vec{R}_{i-1} \cdot \vec{\tilde{n}}\right)\vec{\tilde{n}}. \tag{31}$$

The selection of the free surface cell from the center of which the sub-ray is reflected is done according to the direct search method described in [56]. The Fresnel reflection model is applied for the calculation of the absorption rate as given in [57]:

$$\hat{\alpha} = 1 - \frac{1}{2}\left(\frac{1+(1-\varepsilon\cos\theta_i)^2}{1+(1+\varepsilon\cos\theta_i)^2} + \frac{\varepsilon^2 - 2\varepsilon\cos\theta_i + 2\cos^2\theta_i}{\varepsilon^2 + 2\varepsilon\cos\theta_i + 2\cos^2\theta_i}\right), \tag{32}$$

where ε is a material dependent coefficient taken and modified according to [58] and θ_i is the incident angle at the i-th reflection point. Once all reflections are calculated, the laser power absorbed in each cell is calculated by taking the sum of all sub-ray energies reflecting in the cell and dividing it by the cell volume, V_{cell}:

$$S_{laser}(x,y,z) = \frac{\sum_{j=1}^{755} q_{ray}(x,y)}{V_{cell}}. \tag{33}$$

The second and third term on the RHS of Eq. 27 account for the convection and radiation heat transfer and read:

$$\begin{aligned} q_{convection} &= h_c\left(T - T_{ref}\right), \\ q_{radiation} &= \sigma\varepsilon_r\left(T^4 - T_{ref}^4\right), \end{aligned} \tag{34}$$

where $h_c = 15\ \mathrm{W\,m^{-2}\,K^{-1}}$ is the heat convection coefficient, σ is the Stefan-Boltzmann constant, and ε_r is the emissivity [59]. Note that it is accounted not only for the outward convective and radiative heat fluxes, but as well for the inward heat fluxes due to the high-temperature metal vapor, reaching temperatures of up to 6000 K, known as a secondary heat effect. For this, the reference temperature, T_{ref}, was set to 300 K for the computation of the heat loss by the outward heat fluxes and to 6000 K for the inward heat fluxes [60]. In the present study the range of action for the secondary heat effect was adapted according to the geometrical dimensions of preliminary obtained metallographic cross-sections. The evaporation loss source term is defined according to [61] as:

$$q_{evaporation} = \rho_{liq} h_v F_e, \tag{35}$$

where ρ_{liq} is the liquid density and F_e is the contribution to the speed of the evaporating front only by evaporation. Note that the evaporation loss was considered only for control volumes reaching temperatures above 2700 K since the formulation of the evaporation model is derived for rapid evaporation, thus no diffusive evaporation is accounted for. The critical temperature value of 2700 K has been numerically adapted in such a way that the total amount of heat loss is within the experimentally measured range of up to 3%. The last term on the RHS of Eq. 27 describes the recondensation heat flux. According to [60] a good approximation for the recondensation heat flux is given by considering 18% of the evaporation heat loss calculated in Eq. 35 as local recondensation, and additional 72% which are linearly redistributed as surface heat flux along the keyhole. Note that in the case of partial penetration the recondensation heat is redistributed linearly from zero at the keyhole bottom reaching its maximum value at the keyhole entrance, while in the complete penetration case the amount of recondensation heat at the keyhole exit is 80% of the amount at the keyhole entrance. Furthermore, it is important to mention that all heat fluxes described above have the unit of $\mathrm{W\,m^{-2}}$. Therefore, a transformation term is defined, similar to the one applied in the CSF model, allowing to converse the heat fluxes to power densities with unit of $\mathrm{W\,m^{-3}}$:

$$TT_{energy} = \frac{\rho_{mix} c_{p_{mix}} |\nabla \alpha_{vol_{steel}}|}{\frac{1}{2}\left(\rho_{air} c_{p_{air}} + \rho_{steel} c_{p_{steel}}\right)}, \tag{36}$$

where $c_{p_{air}}$ is the specific heat of air. Hence, the resulting power densities read:

$$S_i = q_i TT_{energy}, \tag{37}$$

where i stands for convection, radiation, evaporation and recondensation.

2.3.3. Boundary conditions

According to the basic principles of fluid-dynamics, and assuming the air phase to be inviscid ($\mu_{air} = 0$) and incompressible, the pressure and viscous stress boundary conditions on the steel-air interface are expressed by the following scalar conditions:

$$p_{air} - p_{steel} + 2\mu_{steel}\frac{\partial \vec{v}_{\vec{\tilde{n}}}}{\partial \vec{\tilde{t}}} = p_{ca} + p_{rec} + p_{vapor}, \tag{38}$$

$$-\mu_{steel}\left(\frac{\partial \vec{v}_{\vec{\tilde{n}}}}{\partial \vec{\tilde{t}}} + \frac{\partial \vec{v}_{\vec{\tilde{t}}}}{\partial \vec{\tilde{n}}}\right) = \tau_{Ma} + \tau_{vapor}. \tag{39}$$

Note that the surface unit normal is directed into the interior of the steel phase, as defined above.

The energy boundary condition on the free surface, considering the multiple Fresnel absorption, heat convection, thermal radiation, evaporation, and recondensation reads:

$$-\lambda_{mix}\frac{\partial T}{\partial \vec{\tilde{n}}} = q_L - q_{convection} - q_{radiation} - q_{evaporation} + q_{recondensation}. \tag{40}$$

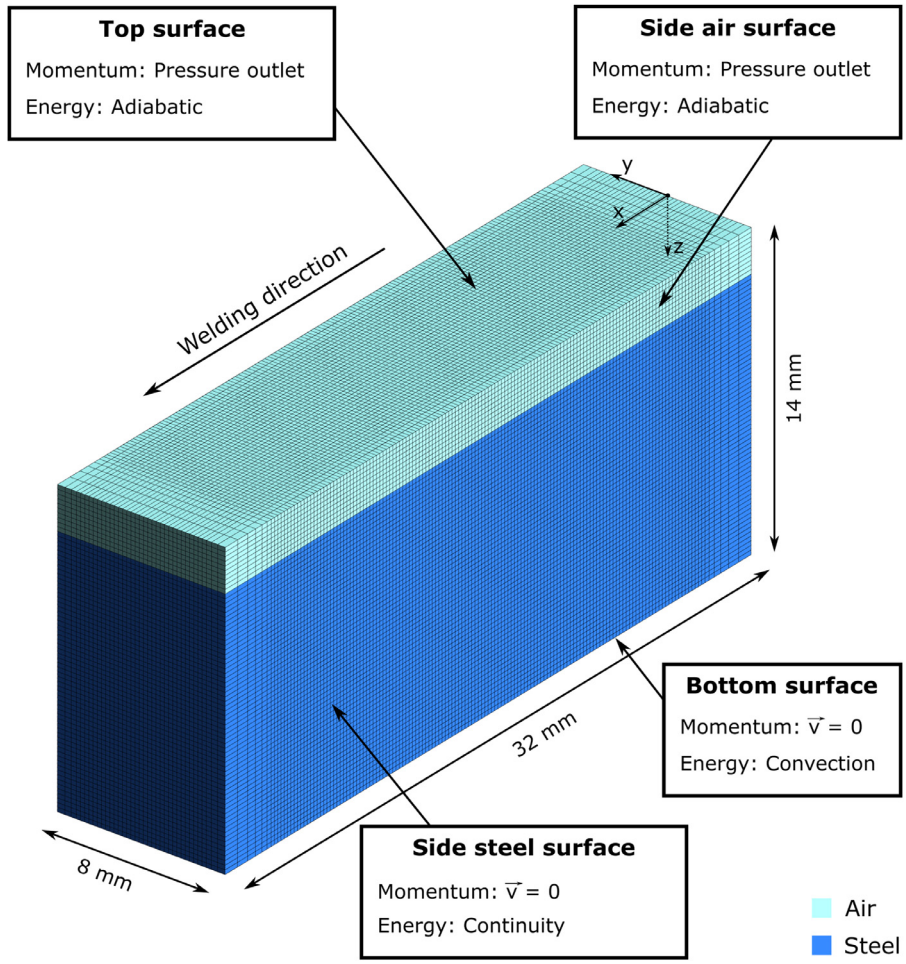

Fig. 3. Boundary conditions of the multi-physics model.

The boundaries of the air-phase domain were set as pressure-outlets; on the bottom of the steel-phase domain convective heat transfer was considered. Note that the simulation domain was chosen to optimize the computational time. Thus, the real steel sheets are much bigger than the considered computational domain. A proper treatment of the boundaries was ensured by implementing the continuity boundary condition proposed in [62]. The boundary conditions can also be found in Fig. 3.

2.3.4. Material properties

The material properties used for the simulation were implemented as temperature-dependent up to the maximum temperature of 3400 K set in the model. Since both materials used are unalloyed steels, the same thermo-physical material properties were used in the model. The base material was modelled as ferritic phase, whereby for temperatures above the austenitization temperature the properties of the austenite phase were taken. The phase or material specific properties were taken from the literature [46,63,64]; if these were not available, the values for pure iron were taken, due to the close chemical composition (Fe $\sim$ 98%). The solid-solid phase transformation (ferrite-austenite) was considered directly in the material properties by including it to the specific heat. However, due to the relatively small amount of the latent heat of the austenite-martensite phase transformation, this was not considered in the model. The thermo-physical material properties are given in Fig. 4. Note that the value for the steel density was calculated as averaged value for the temperature range of interest between 1200 K and 2800 K, giving $\rho_{steel} = 7060\,\mathrm{kg\,m^{-3}}$.

2.3.5. Numerical setup

The computational domain used in the present study has dimensions of 32 mm in length, 8 mm in width and 8 mm or 12 mm in thickness (depending on the thickness of the steel sheets to be welded), see Fig. 3. A finely meshed region with a recommended fixed cell size of 0.2 mm, see [65], was placed between $-2.9\,\mathrm{mm} \leq y \leq 2.9\,\mathrm{mm}$ and $3.0\,\mathrm{mm} \leq x \leq 29\,\mathrm{mm}$. The cell size outside the finely meshed region was defined by a growth rate of 1.1, resulting in a total amount of 372,960 control volumes for the 12 mm thick steel sheets. The weld seam start and end locations were chosen within the finely meshed region at $x = 3.5$ mm and $x = 28.5$ mm, respectively, to assure an error-free selection of the reflection point of the sub-rays. An air layer between $0\,\mathrm{mm} \leq z \leq 2.0\,\mathrm{mm}$ was defined above the steel sheet ($2.0\,\mathrm{mm} \leq z \leq 14.0\,\mathrm{mm}$) allowing to track the free steel-air interface by the VOF method. Note that for the complete penetration calculation an identical air layer was added below the steel sheet. The values of all model parameters are summarized in Section 5.

All governing equations were solved with the commercial finite volume method software ANSYS Fluent. A second order upwind scheme was used for the spatial discretization of the momentum and energy conservation equations and a first order implicit formulation was applied for the discretization of the transient terms. The pressure-velocity coupling was realized by the

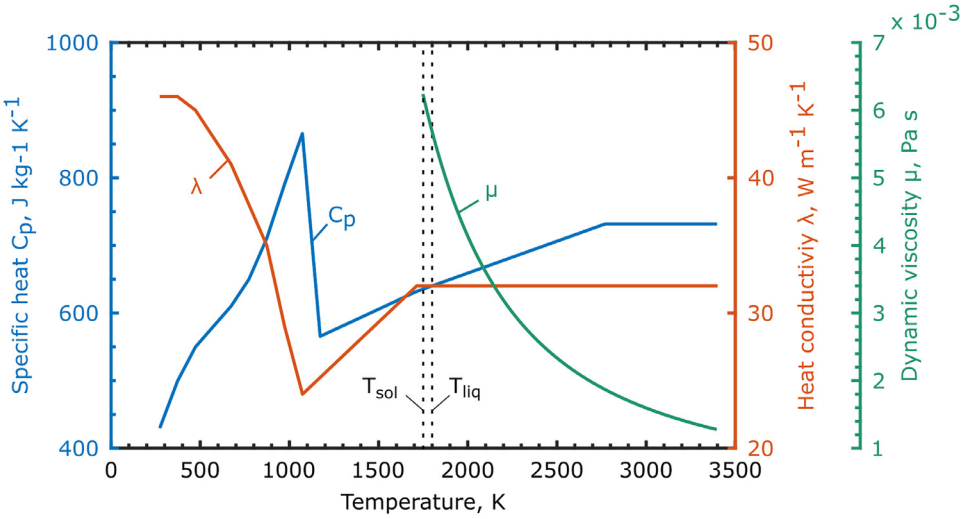

Fig. 4. Thermo-physical material properties for unalloyed steel used in the multi-physics model [46,63,64].

PISO scheme and the steel-air interface was reconstructed by the Geo-Reconstruct method.

A high-performance computing cluster at the Bundesanstalt für Materialforschung und prüfung (BAM) was used for the computation. The averaged computing time was approximately 200 h for 0.6 s real process time.

3. Results

3.1. Validation of the numerical results

Several experimental data have been measured and analysed to ensure the validity of the numerically obtained results according to the ISO/TS 18166 standard [66]. The multi-physics model was initially validated for the 8 mm thick sheets by comparing the averaged drilling time, the weld pool length, the contour of the fusion zone and the time-temperature curves. Once the model was validated, further results, e.g., for 12 mm thick sheets, were verified by comparison of the fusion line and the process efficiency.

3.1.1. Comparison of the averaged drilling time

The measurement of the drilling time by a high speed camera was done according to the experimental setup described in Section 2.2. The experiment was repeated three times to obtain an averaged value for the drilling time at 8 mm thick sheets. The process parameters are given in Table 2. In Fig. 5(a)-(d) four frames captured by the high speed camera from one of the three measurements are shown. Thereby (a) represents the moment right before the laser machine is turned on, (b) the moment of the first reflection on the top surface of the specimen, (c) the moment right before complete penetration is reached, and (d) the moment complete penetration is reached. Since the frame rate was set to 1000, the tolerance of the measurement was exactly 1 ms. The drilling time is estimated from the four frames giving a value of approximately 197 ms. The times from the second and third measurements were approximately 164 ms and 224 ms, respectively. Additionally, the drilling time was estimated according to the thermocouple measurements, see Fig. 2(a)-(b). The complete penetration was reached between the second and third thermocouple on the bottom of the sheet, meaning at about 7 mm after the welding start point. By dividing this value by the welding speed of 33.33 mms^{-1} an approximated drilling time of 210 ms is obtained. An averaged value for the drilling time was calculated from all measured values, resulting in approximately 198 ms. The drilling curve as well as the weld pool shape in the longitudinal section of the numerical model are given in Fig. 5(e). As it can be seen, the drilling period last about 191 ms, which is in very good agreement with the experimentally measured values.

3.1.2. Comparison of the weld pool shape

One of the aims of the numerical model was the accurate prediction of the molten pool and the flow pattern therein. The weld pool interface is defined by the solidus isotherm, T_{sol}, which allows to extract the numerical fusion line from a cross-section as well as the weld pool length on the top surface. In order to account for the experimental tolerances, three metallographic cross-sections were extracted from the quasi-steady state region of the weld seam, according to Fig. 2(c). The shape of the experimental fusion lines for the 8 mm thick sheets is shown in Fig. 6(a)-(c). The experimental tolerance is obtained by overlapping the three fusion lines, as shown in Fig. 6(d). It can be easily seen that the fusion line in Fig. 6(b) is kind of averaged between the fusion lines from Fig. 6(a) and Fig. 6(c). Thus, the numerical fusion line is compared to the experimental average in Fig. 6(e). As seen, the numerical and experimental results show a very good correlation. As described above, the multi-physics model was validated for the partial penetration case of welding 8 mm thick sheets. The numerical results calculated for sheets with a thickness of 12 mm were verified by the comparison of the fusion line shape and the process efficiency. In Fig. 7 the comparison between the experimentally obtained and numerically calculated fusion lines for 12 mm thick sheets is given. As it can be seen there are only minor differences between the fusion lines, resulting due to the tolerances of the experiment and the model. At last, the weld pool shape is validated by comparing the measured and simulated weld pool lengths, see Fig. 8. The numerical model has predicted a weld pool length of 8.2 mm, which is slightly shorter than the experimentally measured value of 8.7 mm. However, it should be mentioned that the weld pool length varied along the weld seam during both, the experiment and the calculation. Thus, the difference of below 5% is considered as a tolerance value.

3.1.3. Comparison of the thermal cycles and the process efficiency

The next validation step is the comparison of the measured and predicted thermal cycles and process efficiency values. The thermal cycles enable the prediction of the local microstructure and

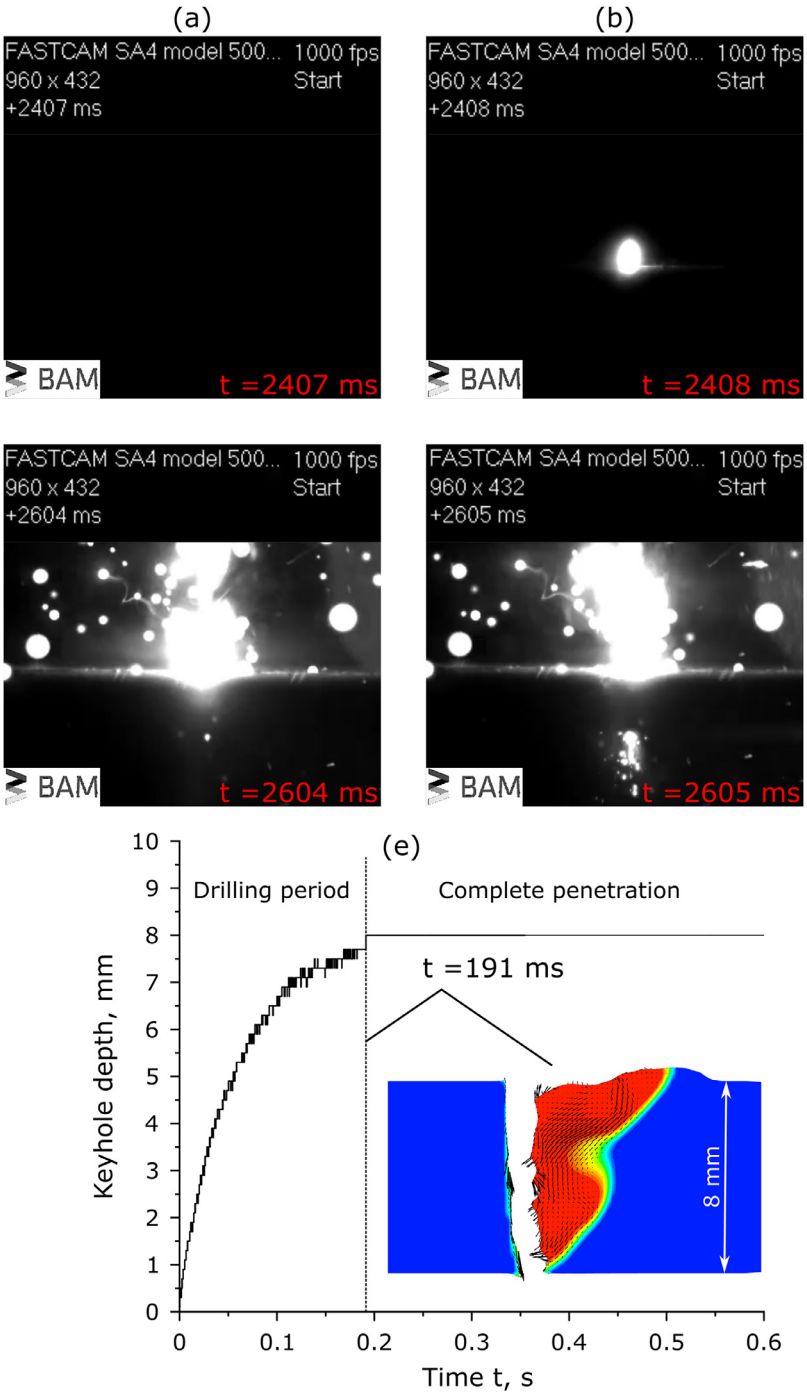

Fig. 5. Measurement of the drilling time by a high speed camera: (a)-(d) experimental, e) numerical drilling time.

the mechanical properties of the part to be welded, thus playing a crucial role in the welding process. Fig. 9 shows the comparison of the measured and calculated time-temperature curve. Note that several time-temperature curves have been obtained experimentally. However, the curve with the maximum measured temperature is chosen for the comparison. It is evident from Fig. 9 that the numerical model captures well the thermal behavior of the welded sheets. In addition to the time-temperature curves, the calculated process efficiency in the model is considered. Fig. 10 shows the amount of absorbed energy during the calculations of the complete and partial penetration cases of 8 mm thick sheets. The average efficiency of the complete and partial penetration simulations were about 79% and 83%, respectively, which is in good agreement with experimental measurements with similar laser powers and process speeds, see, e.g., [67]. Note that the drilling stage of the process was included in the calculation of the averaged values. A closer look at the temporal variation of the absorbed energy shows that the amount of absorbed energy fluctuates more strongly during complete penetration, which is due to the constant opening and closing of the keyhole, known as collapsing. Once the process reaches complete penetration at approximately 200 ms the averaged amount of absorbed energy decreases, leading to the lower total averaged amount. On the other hand, the fluctuations of the absorbed heat during partial penetration are much less, caused

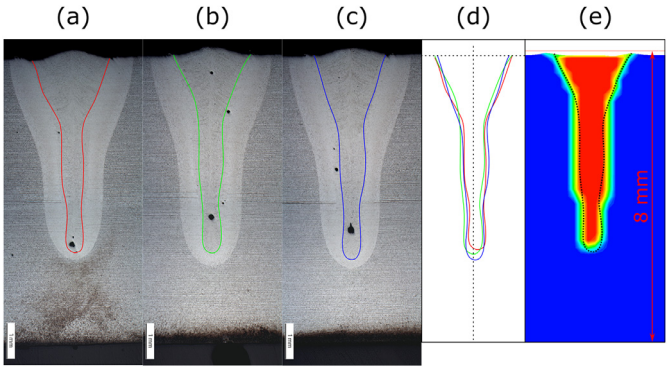

Fig. 6. (a)-(c) show three metallographic cross-sections extracted from the middle of the weld seam of the 8 mm thick sheets. The contour of the fusion line is highlighted by colored lines. In (d) the experimental tolerance range is defined by the overlap of the three fusion lines. (e) shows the comparison of the fusion line from (b) to the calculated fusion line.

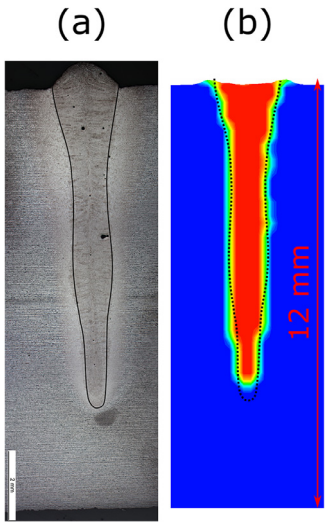

Fig. 7. (a) shows a metallographic cross-section extracted from the middle of the weld seam for 12 mm thick sheets. The contour of the fusion line is highlighted by a black line. (b) shows the comparison of the experimental and numerical fusion lines.

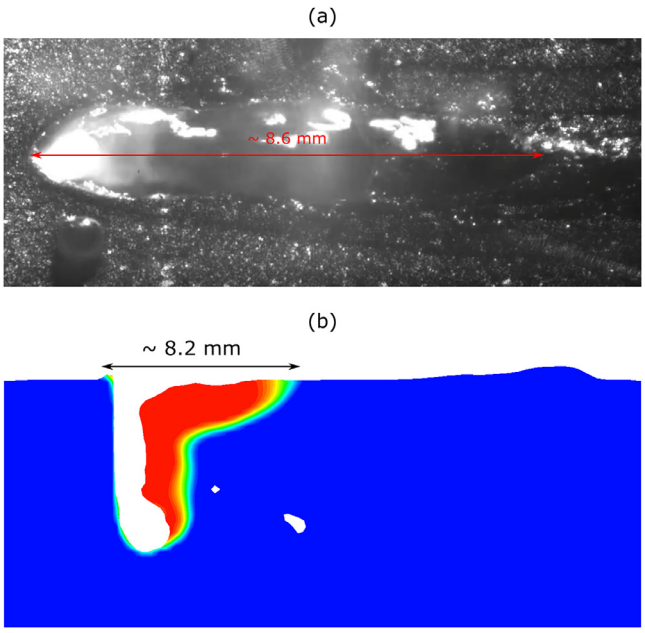

Fig. 8. (a) shows the weld pool length from the middle of the weld seam recorded by the high speed camera. (b) shows the simulated weld pool length at t = 0.33 s.

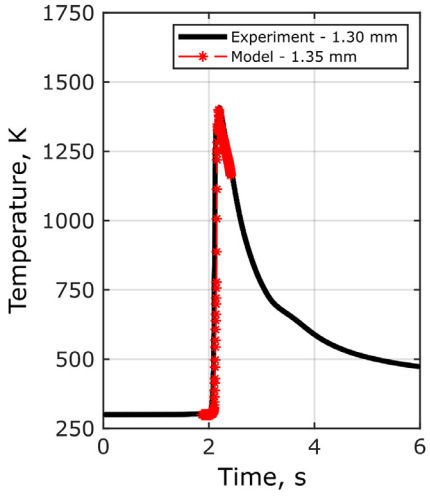

Fig. 9. Comparison of the calculated and experimental thermal cycles on the top surface of the 8 mm thick sheets.

mainly by the fluctuations of the keyhole surface, having direct impact on the multiple reflections.

3.2. Transition behavior of the bulging effect

The dynamic keyhole model described above enabled the study of the fluid flow and thus of the formation of the bulging region. For the estimation of the transition from a slight bulge to a fully developed bulging, which can be considered to have a significant impact on the weld seam quality, several experiments and calculations with different sheet thicknesses and welding parameters for the partial penetration case has been performed.

Based on the numerical results, it was found that the flow pattern in the longitudinal plane of the model is characterised by two vortexes with opposite directions, independently on the presence of a bulge region. The upper part of the weld pool is dominated by the thermo-capillary driven flow leading to an elongated weld pool surface. As seen in Fig. 11 and Fig. 12 the weld pool length depends strongly on the dynamic behavior of the keyhole due to its transient fluctuations and varies along the penetration depth. The vortex in the lower part of the weld pool is comparatively small, caused by the recoil pressure on the keyhole bottom, which depends on the absorbed amount of thermal energy determined by the multiple reflections in the keyhole. The liquid metal in the upper region flows backwards away from the keyhole rear wall, turning downwards and then forward in welding direction approximately at half of the weld pool length. The molten material in the bottom region is pushed backward and redirected by the solid-liquid boundary in upward direction. The two circulations meet and turn their flow directions toward the keyhole rear wall. The cause of the development of a bulging region can be found in the interaction of these circulations. When the subsurface backflow of molten material, which is a consequence of the mass conservation in the top region of the weld pool, and the recoil pressure-induced circulation, tending to move the liquid to the rear part of the weld pool at its bottom, meet, a narrowed region between

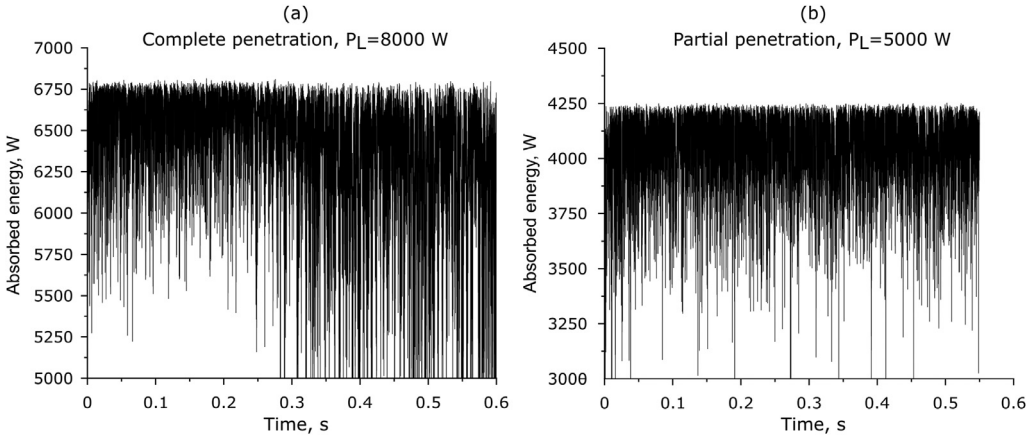

Fig. 10. Amount of absorbed energy computed with the multi-physics model.

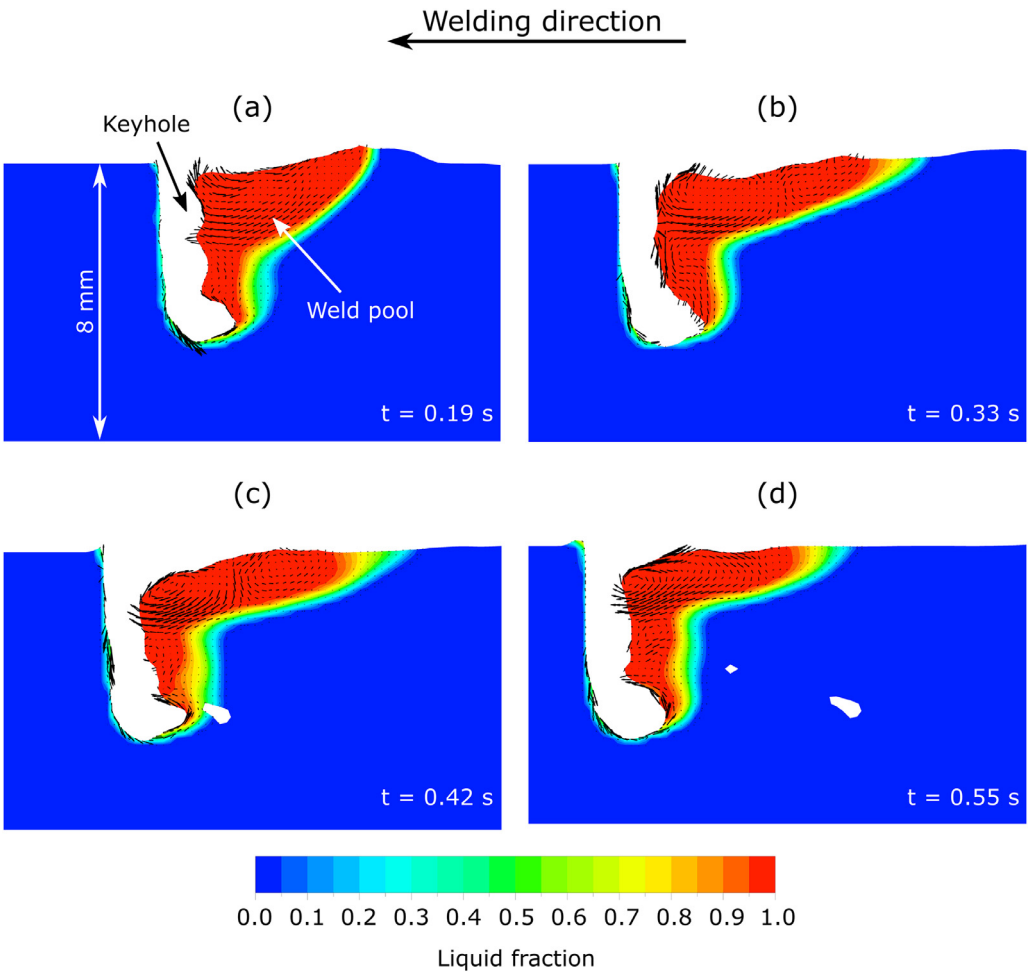

Fig. 11. Temporal evolution of the calculated weld pool shape in the longitudinal plane during partial penetration welding of 8 mm thick sheets.

them is formed. This narrowing effect leads to further separation of the two regions, which results in accumulation of molten material in the bottom region. Hence, the molten material pushed backward from the keyhole bottom causes the elongation of the weld pool interface, called bulging effect.

Although, the flow pattern in the weld pool seem to be independent on the bulge formation, a bulging region is formed once the circulations size and magnitude are high enough. As seen in Fig. 11 and Fig. 12 the flow directions in the longitudinal section are very similar. However, in the case of 8 mm thick sheets, the two vortexes are not sufficiently big and strong to form a nar-

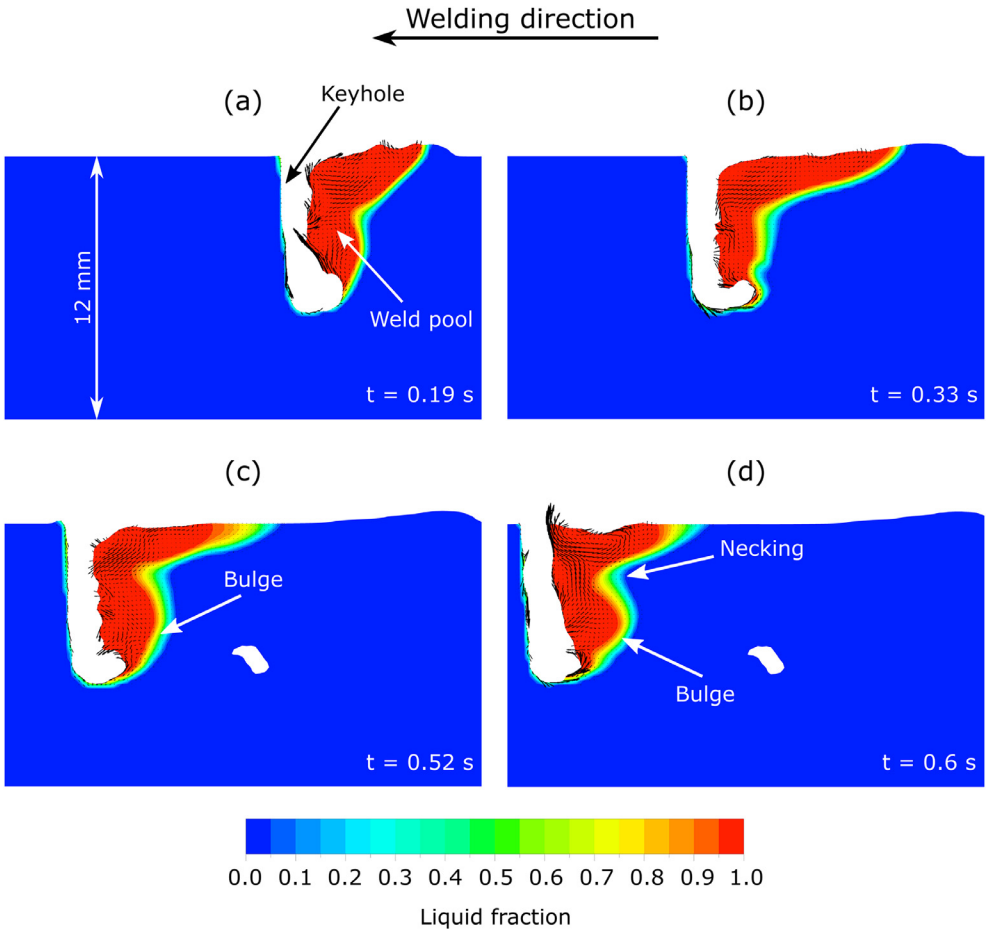

Fig. 12. Temporal evolution of the calculated weld pool shape in the longitudinal plane during partial penetration welding of 12 mm thick sheets.

rowed region between them, which will subsequently contribute to the formation of the bulge. This is as well confirmed by the experimentally obtained depths at which the bulge occurs. The approximate experimental depths of the center of the bulging region for the 8 mm and 12 mm thick sheets are 3.2 mm and 5.2 mm, respectively, see Figs. 6 and 7. Note that these values agree well with the numerically predicted values of 3.8 mm and 4.9 mm for the 8 mm and 12 mm thick sheets, respectively, see Figs. 11 and 12. The lower size and magnitude of the circulations are a result of the lower heat input and penetration depth. Once the laser power is increased for welding the 12 mm thick sheets, the amount of molten material and the penetration depth grow correspondingly. The penetration depth for the 8 mm and 12 mm thick sheets was about 5.7 mm and 9.3 mm, respectively. Hence, the interaction between the vortexes becomes stronger as the penetration depth increases, forming the necking region between them. As shown in Fig. 12(a) the necking forms approximately at the time the weld pool shape reaches a quasi-steady state. A closer look at the results reveals that neither the necking nor the bulging regions seem to be steady-state phenomena. Interestingly, although both occur transiently, they always occur together, as the one may be the cause for the other. Furthermore, according to the numerical results, the bulging in the weld center area forms at penetration depths above 6 mm and occurs much more frequently at penetration depths of about 9 mm. Thus, the transition region from a slight bulge to a fully developed bulging can be numerically estimated to be between 6 mm and 9 mm.

4. Conclusions

In the current work, the formation mechanism of the so-called bulging effect and its transition behavior, or more precisely its dependency on the penetration depth, has been confirmed and studied experimentally as well as numerically. The main conclusions drawn based on the obtained results can be summarized as follow:

- A three-dimensional transient multi-physics numerical model, accounting automatically for the transition from partial to complete penetration, is established, allowing for the prediction of the bulge formation and the study of its behavior.
- Numerous experimental measurements and observations such as drilling time, weld pool length, temperature, efficiency, and metallographic cross-sections are compared to the numerical results showing very good agreement.
- The bulging region forms once the two main circulations in the longitudinal section of the weld pool are separated by a necking region. The necking and bulging regions are found to occur transiently but always together since the former causes the latter and vice versa.
- The bulging effect is strongly dependent on the penetration depth, having its transition from a slight bulge to a fully developed bulging in the range of 6 mm to 9 mm penetration depth.

5. Nomenclature and model parameter values

Latin symbols

Symbol	Unit	Value	Meaning
A	$\sqrt{K}$	0.55	coefficient depending on the ambient pressure
$\hat{A}$	$\mathrm{N\,m^{-1}K^{-1}}$	4.3×10^{-4}	negative slope of the surface tension
A_{mush}	$\mathrm{kg\,m^{-3}\,s^{-1}}$	5×10^{7}	mushy zone constant
a_s	–	0.035	thermodynamic activity
B_0	$\mathrm{kg\,m^{-1}\,s^{-2}}$	3.9×10^{12}	vaporization constant
$c_{p_{air}}$	$\mathrm{J\,kg^{-1}\,K}$	1006	specific heat of air
$c_{p_{mix}}$	$\mathrm{J\,kg^{-1}\,K}$	–	volume-fraction-averaged specific heat
$CSF_{momentum}$	$\mathrm{m^{-1}}$	–	momentum transformation term
D	m	–	averaged keyhole diameter
D_{sub}	m	1.61×10^{-5}	length of the ray tracing sub-regions
d	m	124.1×10^{-12}	molecular diameter of iron
f	–	–	term determined by the flow pattern
F_c	–	0.48	coherent solid fraction
F_{cr}	–	0.64	critical solid fraction
F_l	$\mathrm{ms^{-1}}$	–	contribution to the speed of the evaporating front
F_s	–	–	solid fraction
$\vec{g}$	$\mathrm{ms^{-2}}$	$(0, 0, 9.81)$	gravitational acceleration vector
ΔH_0	$\mathrm{J\,mol^{-1}}$	-1.66×10^{-5}	standard heat of adsorption
H_{mix}	J	–	volume-fraction-averaged enthalpy
h_c	$\mathrm{W\,m^{-2}K^{-1}}$	15	heat convection coefficient
h_{depth}	m	–	keyhole depth
h_f	$\mathrm{J\,kg^{-1}}$	247×10^{3}	latent heat of fusion of unalloyed steel
h_{mix}	$\mathrm{J\,kg^{-1}}$	–	volume-fraction-averaged sensible enthalpy
h_{ref}	$\mathrm{J\,kg^{-1}}$	–	sensible enthalpy at the reference temperature
h_v	$\mathrm{J\,kg^{-1}}$	6260×10^{3}	latent heat of vaporization of unalloyed steel
i	–	–	running index
k_b	$\mathrm{J\,K^{-1}}$	1.381×10^{-23}	Boltzmann constant
k_l	–	3.18×10^{-3}	constant related to the entropy of segregation
L	$\mathrm{J\,kg^{-1}}$	–	latent heat content
M_{mol}	$\mathrm{kg\,mol^{-1}}$	55.845×10^{-3}	molar mass of pure iron
$\vec{n}$	m	–	surface normal vector
$\vec{\hat{n}}$	–	–	surface unit normal vector
p	$\mathrm{N\,m^{-2}}$	–	fluid pressure
p_{air}	$\mathrm{N\,m^{-2}}$	–	air pressure at the steel-air interface
p_{ca}	$\mathrm{N\,m^{-2}}$	–	capillary pressure
P_L	W	see Table 2	laser power
P_{ray}	W	–	sub-ray power
p_{rec}	$\mathrm{N\,m^{-2}}$	–	recoil pressure
p_{steel}	$\mathrm{N\,m^{-2}}$	–	steel pressure at the steel-air interface
p_{vapor}	$\mathrm{N\,m^{-2}}$	–	stagnation pressure due to the metal vapor
$q_{convection}$	$\mathrm{W\,m^{-2}}$	–	convective heat flux density
$q_{evaporation}$	$\mathrm{W\,m^{-2}}$	–	evaporative heat flux density
q_L	$\mathrm{W\,m^{-2}}$	–	laser heat flux density
$q_{radiation}$	$\mathrm{W\,m^{-2}}$	–	radiative heat flux density
$\hat{R}_g$	$\mathrm{J\,mol^{-1}K^{-1}}$	8.314×10^{-3}	universal gas constant
$\vec{R}_i$	m	–	direction vector of the i-th sub-ray reflection
r_{f_0}	m	5×10^{-4}	laser beam radius at the focal plane
$r_f(z)$	m	–	laser beam radius along the optical axis
$S_{convection}$	$\mathrm{W\,m^{-3}}$	–	convection power density
S_e	$\mathrm{W\,m^{-3}}$	–	energy source term
$S_{evaporation}$	$\mathrm{W\,m^{-3}}$	–	evaporation power density
$S_{radiation}$	$\mathrm{W\,m^{-3}}$	–	radiation power density
$S_{recondensation}$	$\mathrm{W\,m^{-3}}$	–	recondensation power density
S_{laser}	$\mathrm{W\,m^{-3}}$	–	laser power density
$\vec{S}_m$	$\mathrm{N\,m^{-3}}$	–	momentum source term
$\vec{S}_{rec}$	$\mathrm{N\,m^{-3}}$	–	volume force of the recoil pressure
$\vec{S}_{shear}$	$\mathrm{N\,m^{-3}}$	–	volume force of the vapor-induced shear stress
$\vec{S}_{stagnation}$	$\mathrm{N\,m^{-3}}$	–	volume force of the vapor-induced stagnation pressure
$\vec{S}_{surf.tension}$	$\mathrm{N\,m^{-3}}$	–	volume force of the surface tension
$\vec{S}_{vapor}$	$\mathrm{N\,m^{-3}}$	–	volume force due to the metal vapor
T	K	–	temperature
T_{liq}	K	1800	liquidus temperature
T_{max}	K	3400	maximum temperature
T_{ref}	K	300	reference temperature
T_{sol}	K	1750	solidus temperature
TT_{energy}	$\mathrm{m^{-1}}$	–	energy transformation term
t	s	–	time
$\vec{v} = (v_x, v_y, v_z)$	$\mathrm{ms^{-1}}$	–	fluid velocity vector
$\vec{V}$	$\mathrm{ms^{-1}}$	$(0, 0, -150)$	vapor velocity vector - partial penetration; origin at keyhole bottom
$\vec{V}$	$\mathrm{ms^{-1}}$	$(0, 0, -150)$ $(0, 0, 100)$	vapor velocity vector - complete penetration; origin at two-thirds of the plate thickness
V_{cell}	$\mathrm{m^{-3}}$	8×10^{-12}	cell volume
V_{key}	$\mathrm{m^{-3}}$	–	keyhole volume
$\vec{v}_{\vec{n}}$	$\mathrm{ms^{-1}}$	–	normal projection of the vapor velocity vector
$\vec{v}_{\vec{t}}$	$\mathrm{ms^{-1}}$	–	tangential projection of the vapor velocity vector
x, y, z	m	–	Cartesian frame coordinates
z_0	m	2×10^{-3}	position of the focal plane along the optical axis
z_r	m	see Table 2	Rayleigh legnth

Greek symbols

Symbol	Unit	Value	Meaning
$\hat{\alpha}$	–	–	absorption rate
α_{liq}	–	–	liquid volume fraction
$\alpha_{vol_{steel}}$	–	–	volume fraction of the steel phase
β_{steel}	$\mathrm{K^{-1}}$	1.6×10^{-5}	volumetric thermal expansion coefficient of pure iron
Γ_s	$\mathrm{mol\,m^{-2}}$	1.3×10^{-5}	surface excess at saturation
γ	$\mathrm{N\,m^{-1}}$	–	surface tension
γ_0	$\mathrm{N\,m^{-1}}$	1.943	surface tension of pure iron
ε	$\mathrm{N\,m^{-1}K^{-1}}$	0.25	material dependent coefficient
ε_r	–	0.4	emissivity
ϵ	–	1×10^{-3}	numerical constant
θ_i	rad	–	incident angle at the i-th reflection point
κ	$\mathrm{m^{-1}}$	–	curvature
λ_{air}	$\mathrm{W\,m^{-1}K^{-1}}$	2.42×10^{-2}	heat conductivity of air
λ_{vapor}	$\mathrm{W\,m^{-1}K^{-1}}$	5×10^{-1}	heat conductivity of metal vapor
λ_{mix}	$\mathrm{W\,m^{-1}K^{-1}}$	–	volume-fraction-averaged heat conductivity
μ_{air}	Pas	1.79×10^{-5}	dynamic viscosity of air
μ_{mix}	Pas	–	volume-fraction-averaged dynamic viscosity
μ_{steel}	Pas	–	effective dynamic viscosity for the steel phase
$\mu_{T_{max}}$	Pas	1.62×10^{-4}	dynamic viscosity of metal vapor at T_{max}
μ_0	Pas	5.7×10^{-3}	dynamic viscosity at T_{liq}
ρ_{air}	$\mathrm{kg\,m^{-3}}$	1.225	mass density of air
ρ_{liq}	$\mathrm{kg\,m^{-3}}$	7060	mass density of liquid steel

(continued on next page)

ρ_{mix}	$kg\,m^{-3}$	–	volume-fraction-averaged mass density
ρ_{steel}	$kg\,m^{-3}$	7060	mass density of steel
ρ_{vapor}	$kg\,m^{-3}$	1.13×10^{-4}	mass density of metal vapor
σ	$W\,m^{-2}K^{-4}$	5.67×10^{-8}	Stefan-Boltzmann constant
$\hat{\sigma}$	m^2	–	collision cross-section of an iron molecule
τ_{Ma}	$N\,m^{-2}$	–	Marangoni shear stress
τ_{vapor}	$N\,m^{-2}$	–	vapor-induced shear stress

Abbreviations	
BAM	Bundesanstalt für Materialforschung und -prüfung
CSF	Continuum surface force
EHS	Equivalent heat source
RHS	Right hand side
VOF	Volume of fluid

Declaration of Competing Interest

The authors declare no conflict of interest. The funders had no role in the design of the study; in the collection, analyses, or interpretation of data; in the writing of the manuscript, or in the decision to publish the results.

Acknowledgments

This work is funded by the Deutsche Forschungsgemeinschaft (DFG, German Research Foundation) project Nr. 411393804 (BA 5555/5-1) and Nr. 416014189 (BA 5555/6-1).

References

[1] M. Bachmann, A. Gumenyuk, M. Rethmeier, Welding with high-power lasers: Trends and developments, Physics Procedia 83 (2016) 15–25.
[2] X. Zhang, E. Ashida, S. Tarasawa, Y. Anma, M. Okada, S. Katayama, M. Mitzutani, Welding of thick stainless steel plates up to 50 mm with high brightness lasers, Journal of Laser Applications 23 (2011) 022002.
[3] A. Fritzsche, V. Avilov, A. Gumenyuk, K. Hilgenberg, M. Rethmeier, M. High, power laser beam welding of thick-walled ferromagnetic steels with electromagnetic weld pool support, Phys. Procedia 83 (2016) 362–372.
[4] J.F. Ready, D.F. Farson, LIA handbook of laser materials processing, 2001, Laser Institute of America, Orlando.
[5] J. Schuster, S. Keitel, E. Schulze, H. Maly, Fachbeiträge-entstehung erstarrungsbedingter risse in laserstrahlschweissverbindungen an unlegierten und niedriglegierten baustahlen, Schweien und Schneiden 51 (1999) 252–257.
[6] J. Schuster, Heirisse in schweiverbindungen: Entstehung, nachweis und vermeidung, DVS-Verlag (2004).
[7] M.O. Gebhardt, A. Gumenyuk, M. Rethmeier, Numerical analysis of hot cracking in laser hybrid welded tubes, Advances in Materials Science and Engineering (2004) 520786.
[8] M. Rappaz, J. Dantzig, Solidification, first, EFPL Press (2009).
[9] J. Lippold, Welding metallurgy and weldability, first, John Wiley & Sons (2014).
[10] C. Cross, On the origin of weld solidification cracking, In Hot cracking phenomena in welds. Springer (2005) 3–18.
[11] A. Artinov, N. Bakir, M. Bachmann, A. Gumenyuk, M. Rethmeier, Weld pool shape observation in high power laser beam welding, Procedia CIRP 74 (2018) 683–686.
[12] T. Shida, H. Okumura, Y. Kawada, Effects of welding parameters and prevention of defects in deep penetration electron beam welding of heavy section steel plates, Weld. World 17 (1979) 196–207.
[13] S. .Tsukamoto, H. Irie, M. Inagaki, Welding defects and molten metal behaviour in electron beam welding, The fourth international Symposium of the Japan Welding Society (1982) 115–120.
[14] S. Tsukamoto, H. Irie, Welding defects and molten metal behaviour in low speed electron beam welding, Welding in the World (1985) 130–140.
[15] S. Tsukamoto, H. Irie, Mechanism of locally delayed solidification in electron beam welding, Welding international 5 (1991) 177–183.
[16] A. Artinov, N. Bakir, M. Bachmann, A. Gumenyuk, S.J. Na, M. Rethmeier, On the search for the origin of the bulge effect in high power laser beam welding, Journal of Laser Applications 31 (2) (2019) 022413.
[17] L.D. Barbetta, Solidification flaw and porosity formation in hybrid laser: GMA welding of thick API 5l x70 steel plates, 2014,
[18] L.D. Barbetta, W.L. Weingaertner, O. Seffer, R. Lahdo, S. Kaierle, S. Influence of molten pool geometry and process parameters on solidification cracsk formation in hybrid laser-GMA welding of thick 5L X70 steel plates, In ABCM International Congress of Manufacturing Engineering (COBEM), 8th Brazilian Congress of Manufacturing Engineering (2015).
[19] W.-I. Cho, S.-J. Na, C. Thomy, F. Vollertsen, Numerical simulation of molten pool dynamics in high power disk laser welding, Journal of Materials Processing Technology 212 (2012) 262–275.
[20] M. Bachmann, V. Avilov, A. Gumenyuk, M. Rethmeier, Experimental and numerical investigation of an electromagnetic weld pool support system for high power laser beam welding of austenitic stainless steel, Journal of Materials Processing Technology 214 (3) (2014a) 578–591.
[21] M. Bachmann, V. Avilov, A. Gumenyuk, M. Rethmeier, Experimental and numerical investigation of an electromagnetic weld pool control for laser beam welding, Physics Procedia 56 (2014b) 515–524.
[22] M. Sohail, S.-W. Han, S.-J. Na, A. Gumenyuk, M. Rethmeier, Numerical investigation of energy input characteristics for high-power fiber laser welding at different positions, International Journal of Advanced Manufacturing Technology 80 (2015) 931–946.
[23] F. Lu, X. Li, Z. Li, X. Tang, H. Cui, Formation and influence mechanism of keyhole-induced porosity in deep-penetration laser welding based on 3d transient modeling, International Journal of Heat and Mass Transfer 90 (2015) 1143–1152.
[24] M. Bachmann, R. Kunze, V. Avilov, M. Rethmeier, Finite element modeling of an alternating current electromagnetic weld pool support in full penetration laser beam welding of thick duplex stainless steel plates, Journal of Laser Applications 28 (2) (2016) 022404.
[25] Z. Gao, P. Jiang, G. Mi, L. Cao, W. Liu, Investigation on the weld bead profile transformation with the keyhole and molten pool dynamic behavior simulation in high power laser welding, International Journal of Heat and Mass Transfer 116 (2018) 1304–1313.
[26] M.O. Gebhardt, Einfluss von konstruktion und schweiparametern auf die erstarrungsrissentstehung beim laser-MSG-hybridschweien dickwandiger bauteile experimentelle und numerische analyse. Bundesanstalt für Materialforschung und prüfung (BAM), 2014.
[27] D. Radaj, H. Häuser, S. Braun, Numerische simulation von eigenspannungen und verzug bei schweiverbindungen aus almgsi-legierungen, Konstruktion 50(7-8) (1998) 31–37.
[28] A. Artinov, M. Bachmann, M. Rethmeier, Equivalent heat source approach in a 3d transient heat transfer simulation of full-penetration high power laser beam welding of thick metal plates, International Journal of Heat Mass Transfer 122 (2018) 1003–1013.
[29] N. Bakir, A. Artinov, A. Gumenyuk, M. Bachmann, M. Rethmeier, Numerical simulation on the origin of solidification cracking in laser welded thick-walled structures, Metals 8 (6) (2018) 406.
[30] A. Artinov, V. Karkhin, N. Bakir, M. X, M. Bachmann, A. Gumenyuk, M. Rethmeier, Lam curves approximation for the assessment of the 3-d temperature distribution in keyhole mode welding processes, Journal of Laser Applications 32 (2) (2020) 022024.
[31] A. Artinov, V. Karkhin, P. Khomich, M. Bachmann, M. Rethmeier, Assessment of thermal cycles by combining thermo-fluid dynamics and heat conduction in keyhole mode welding processes, International Journal of Thermal Sciences 145 (2019) 105981.
[32] A. Artinov, M. Bachmann, X. Meng, V. Karkhin, M. Rethmeier, On the relationship between the bulge effect and the hot cracking formation during deep penetration laser beam welding, Procedia CIRP 94 (2020) 5–10.
[33] S. Kou, s. Welding Metallurgy, John Wiley & Sons (2003).
[34] M.E. Glicksman, Principles of solidification: An introduction to modern casting and crystal growth concepts, Springer New York (2011).
[35] X. Meng, M. Bachmann, A. Artinov, M. Rethmeier, Experimental and numerical assessment of weld pool behavior and final microstructure in wire feed laser beam welding with electromagnetic stirring, Journal of Manufacturing Processes 45 (2019a) 408–418.
[36] X. Meng, A. Artinov, M. Bachmann, M. Rethmeier, Numerical and experimental investigation of thermo-fluid flow and element transport in electromagnetic stirring enhanced wire feed laser beam welding, International Journal of Heat Mass Transfer 144 (2019b) 118663.
[37] X. Meng, A. Artinov, M. Bachmann, M. Rethmeier, Numerical study of additional element transport in wire feed laser beam welding, Procedia CIRP 94 (2020a) 722–725.
[38] X. Meng, A. Artinov, M. Bachmann, M. Rethmeier, Theoretical study of influence of electromagnetic stirring on transport phenomena in wire feed laser beam welding, Journal of Laser Applications 32 (2) (2020b) 022026.
[39] X. Meng, M. Bachmann, A. Artinov, M. Rethmeier, The influence of magnetic field orientation on metal mixing in electromagnetic stirring enhanced wire feed laser beam welding, Journal of Materials Processing Technology 294 (2021) 117135.
[40] C.W. Hirt, B.D. Nichols, Volume of fluid (VOF) method for the dynamics of free boundaries, Journal of Computational Physics (1981) 201–225.
[41] D.L. Youngs, Time-dependent multi-material flow with large fluid distortion, Numerical Methods for Fluid Dynamics 24 (1982) 273–285.
[42] T.E. Faber, Fluid dynamics for physicists, Cambridge University Press (1995).
[43] V.R. Voller, C. Prakash, A fixed grid numerical modelling methodology for convection-diffusion mushy region phase-change problems, International journal of heat and mass transfer 30 (8) (1987) 1709–1719.
[44] A.D. Brent, V.R. Voller, K.T.J. Reid, Enthalpy-porosity technique for modeling convection-diffusion phase change: application to the melting of a pure metal, Numerical Heat Transfer, Part A Applications 13 (3) (1988) 297–318.

[45] M.H. Cho, Y.C. Lim, D.F. Farson, Simulation of weld pool dynamics in the stationary pulsed gas metal arc welding process and final weld shape, Welding Journal New-York 85 (12) (2006) 271–283.
[46] P. Sahoo, T. Debroy, M.J. McNallan, Surface tension of binary metal-surface active solute systems under conditions relevant to welding metallurgy, Metallurgical transactions B 19 (3) (1988) 483–491.
[47] J.U. Brackbill, D.B. Kothe, C. Zemach, A continuum method for modeling surface tension, Journal of Computational Physics 100 (1992) 335–354.
[48] V. Semak, A. Matsunawa, The role of recoil pressure in energy balance during laser materials processing, Journal of Physics D-Applied Physics (1997) 2541.
[49] F.M. White, Fluid mechanics froth edition, McGraw-Hill, New York (1999).
[50] E.H. Amara, A. Bendib, Modelling of vapour flow in deep penetration laser welding, Journal of Physics D-Applied Physics 35 (2002) 272–280.
[51] D. Wu, X. Hua, F. Li, L. Huang, Understanding of spatter formation in fiber laser welding of 5083 aluminum alloy, International Journal of Heat and Mass Transfer 113 (2017) 730–740.
[52] R. Zhang, X. Tang, L. Xu, F. Lu, H. Cui, Study of molten pool dynamics and porosity formation mechanism in full penetration fiber laser welding of al-alloy, International Journal of Heat and Mass Transfer 148 (2020) 119089.
[53] W. Tan, N.S. Bailey, C.S. Yung, Investigation of keyhole plume and molten pool based on a three-dimensional dynamic model with sharp interface formulation, Journal of Physics D: Applied Physics 46 (5) (2013) 055501.
[54] W. Tan, C.S. Yung, Analysis of multi-phase interaction and its effects on keyhole dynamics with a multi-physics numerical model, Journal of Physics D: Applied Physics 47 (34) (2014) 345501.
[55] G.P. Sasmal, Numerical modeling of thermocapillary convection with curved and deforming free surfaces, [Ph.D.], Memphis State University, Ann Arbor (1993).
[56] S.-W. Han, A. Junsu, S.J. Na, A study on ray tracing method for CFD simulations of laser keyhole welding: progressive search method, Welding in the World 60, no. 2 (2016) 247–258.
[57] W. Schulz, G. Simon, H.M. Urbassek, L. Decker, On laser fusion cutting of metals, Journal of Physics D-Applied Physics 20 (1987) 481–488.
[58] R. Ducharme, K. Williams, P. Kapadia, J. Dowden, B. Steen, M. Glowacki, The laser welding of thin metal sheets: an integrated keyhole and weld pool model with supporting experiments, Journal of physics D: Applied physics 27 (8) (1994) 1619.
[59] T.L. Bergman, F.P. Incropera, Fundamentals of heat and mass transfer, John Wiley & Sons (2011).
[60] S. Muhammad, S. Han, S.J. Na, A. Gumenyuk, M. Rethmeier, Study on the role of recondensation flux in high power laser welding by computational fluid dynamics simulations, Journal of Laser Application 30 (2018) 012013.
[61] H. Ki, P.S. Mohanty, J. Mazumder, Modelling of high-density laser-material interaction using fast level set method, Journal of Physics D: Applied Physics 34 (3) (2001) 364–372.
[62] X. Meng, G. Qin, R. Zong, Thermal behavior and fluid flow during humping formation in high-speed full penetration gas tungsten arc welding, International Journal of Thermal Science 134 (2018) 380–391.
[63] K.C. Mills, Recommended values of thermophysical properties for selected commercial alloys, Woodhead Publishing (2002).
[64] Material database, 2009, ESI Group.
[65] W.I..N. Cho, S.J. Impact, of wavelengths of CO_2, disk, and green lasers on fusion zone shape in laser welding of steel, J. Weld. Join. 38 (2020) 235–240.
[66] ISO/TS 18166:2016 Numerical welding simulation Execution and documentatio.
[67] Y. Kawahito, N. Matsumoto, Y. Abe, S. Katayama, Relationship of laser absorption to keyhole behavior in high power fiber laser welding of stainless steel and aluminum alloy, Journal of Materials Processing Technology 211 (10) (2011) 1563–1568.